DIPARTIMENTO DI MECCANICA

mecc

Limitations of the inherent strain method in simulating powder bed fusion processes

Bugatti, Matteo; Semeraro, Quirico

Limitations of the Inherent Strain Method in Simulating Powder Bed Fusion Processes

Matteo Bugatti[a,*], Quirico Semeraro[a]

[a]*Dipartimento di Meccanica, Politecnico di Milano, via La Masa 1, 20156, Milano (MI), Italy*

Abstract

Process optimization has always been a crucial step for effective usage of metal additive manufacturing (AM) processes: it consists in establishing quantitative relations between final part's characteristics and process parameters to find their optimal combination and obtain a fully functional mechanical component. Experimental investigation techniques are usually employed for this purpose but they can be extremely expensive and time-consuming, especially when the output of the process depends on a large number of parameters, like for AM. Numerical simulation could represent an alternative solution: by reproducing the real process characteristics, a simulation could provide useful insights, allowing to evaluate the performance of the process for different parameter combinations without relying exclusively on expensive experimental campaigns.

In this work, a finite element AM simulation based on the Inherent Strain (IS) method was developed and the prediction performance in terms of part's residual deformation was evaluated by comparing the numerical results with the measurements carried out on an experimental campaign. A new model calibration approach for prediction improvement was also implemented and it allowed to discover an unexpected behaviour of the model that strongly affects the validity of this method for AM simulation.

1. Problem Statement

In the last years, Additive Manufacturing (AM) processes gained popularity in manufacturing industry thanks to their unmatched characteristics in terms of product design flexibility. However, a few key issues (e.g. dimensional accuracy, residual tension, porosities) affect the final products and they are limiting the diffusion of this new technology. For this reason, process optimization is always required to produce a fully functional mechanical component: it consists in testing different combinations of process parameters to find the optimal process window, that is the parameters combination region that meets the performance requirements. There are many different parameters that must be set for an AM process, a few of them are reported in the following list:

- scan strategy (path and speed);

- pre-heating temperature;

- layer thickness;

- beam size and power;

- powder size and morphology;

Their influence on the output quality of every new build should be carefully evaluated. This is clearly a multi-variable problem because the process window for the production of each component will be a specific combination of the aforementioned parameters.

Today's process optimization is exclusively carried out relying on expensive experimental campaigns. This approach has the advantage of being the most accurate solution, since results come directly from the machine, but it is a slow iterative approach which is highly expensive both in terms of times and costs because it relies on quality measurements of parts which must be directly built, thus wasting material and energy. For these reasons, a new process optimization approach based on simulation would be extremely appealing. Following the same iterative optimization path, it would allow to avoid all the wastes (build/quality measuring costs and times) of the test-based approach, supporting the design with useful process insights by simulating the process performance with different combinations of process parameters without building the component. The fully functional part can then be built the "first time right", once its production is optimized. In this work, the AM simulation topic is thoroughly discussed and the capabilities of this kind of approach in improving the process design are evaluated and directly tested by developing a new AM

---

*Corresponding author

Email addresses: matteo.bugatti@polimi.it (Matteo Bugatti), quirico.semeraro@polimi.it (Quirico Semeraro)

simulation model.

The paper is focused on obtaining an accurate prediction of the residual stress state of the built component. This output determines the final part deformation and cracks formation, which are two of the most critical defects that must be avoided with proper process design.

For validation purposes, all the simulation results were compared to the deformation measurements of real parts built with a laser-based Powder Bed Fusion (PBF) (a.k.a. SLM) machine, the Renishaw AM250 SLM System, and studied in a recent experimental campaign described in Appendix A.

The paper is organized as follows:

- in **Section 2**, a comparison and a classification of the models described in literature is carried out, evaluating the features that an AM process simulation should have.

- In **Section 3**, a complete characterization of the process is made to define the simulation input parameters (material properties, thermal boundary conditions, process parameters) and the numerical AM model studied in this paper is thoroughly described both in terms of applied method and implementation.

- In **Section 4**, the numerical results of each model are discussed using the data obtained from an experimental campaign to validate and evaluate the performance of the developed model. At last, different approaches are compared to improve the simulation prediction accuracy.

- In **Section 5**, based on the results obtained throughout the work, general conclusions are drawn about the strengths and the limitations of the developed AM simulation. In addition, some suggestions for further improvements are reported and a possible research path is traced for future developments on this topic.

2. State of the Art

Despite being a relatively new topic, due to its industrial appealing, AM simulation literature is already vast. Researchers have come up with several possible solutions, which have been categorized in Fig. 1: for each category, in round brackets, it is reported the employed numerical method, which depends on the simulated process and on the desired output, and in squared brackets the number of papers analysed for each category. Before creating a new simulation, all the possible options have been considered.

Micro-scale models were found to be capable of predicting local defects formation mechanisms and instabilities (e.g. porosity, spatter, denudation and balling) correlating them to specific combinations of process parameters [1, 2, 3, 4]. These complex multiphysics models simulate a large number
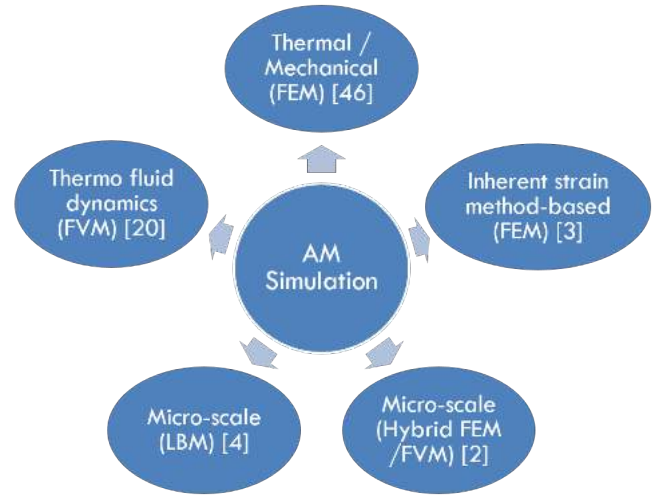
Figure 1: Literature solutions for AM simulation

of process-related thermo-fluid dynamics phenomena (conductivity, molten pool convective flow, wettability, capillary/thermo-capillary forces, plasma plume recoil pressure etc.) but they require extensive computational power: only extremely small domains and time periods can be simulated with these models in reasonable times (in the order of few ms and a fraction of mm^3). In addition, they are developed with non-standard numerical methods (e.g. LBM = Lattice Boltzmann Method) implemented in unavailable, closed-source codes or proprietary software: therefore, this option could not be further investigated.

Thermo-mechanical finite element method (FEM) models couple the thermal and the mechanical aspect of the process within a single simulation. By defining the thermo-mechanical properties of the material, it is possible to find the temperature induced stress and deformation state at each time frame of the transient simulation. With this kind of coupled analysis, the viscous dissipation phenomenon can be taken into account. During the process, in fact, the thermal field is influenced by the heat generated by the plastic deformation. Its contribution to the temperature field can be modelled as an additional volumetric heat flux by implementing a proper strain hardening model.

Shen and Chou [5] ran a 2 layers, small-scale (4×2 mm) coupled thermo-mechanical simulation. The powder/solid phase-change is implemented together with an unspecified model that takes into account the viscous dissipation. However, the mechanical behaviour of the powder is not clearly outlined and the results are only validated with literature data.

Labudovic and Hu [6] developed a small single-scan multi-layer direct energy deposition (DED) simulation. Continuous material addition is implemented but powder behaviour is not modelled. The output of the simulation is directly validated measuring the molten pool size and the residual stresses.

Aggarangsi [7] simulated the effect of DED localized preheating on the final stress distribution in a simple 2D analysis. Continuous material addition is not

implemented and no experimental validation is presented.

Denlinger and Irwin [8] developed a 107 layers model to predict the distortion of the working plate. The results are validated by measuring the distortion of the real part. Quiet layer activation is implemented but specific powder properties are not considered.

Zhang and Chou [9] studied a DED process implementing the additive mechanism. Sensitivity of the numerically computed distortion to different process parameters is studied but details about the implementation are not provided.

Hussein [10] studied the effects of process parameters on the temperature distribution, melt pool size and thermal stress. Powder properties and the additive mechanism are also considered but only a single layer scanning is simulated.

All the papers presented here simulate the addition of real micro layers which are sequentially activated and scanned by a realistic energy source in a layer-by-layer fashion. However, most of the models simulate the building of a few layers of thin walls or small blocks. This is because the increased complexity of the problem requires extensive computational power to handle the material non-linearity, state and phase change for a coupled thermo-mechanical analysis. This kind of simulation approach seems to be not applicable to bigger models.

Another drawback of thermal models is the incomplete addressing of the fluid-dynamics aspects of the process. Within the molten pool, liquid metal fluxes arise due to the forces acting on the fluid. Heat exchange behaviour deeply influences the efficiency and the evolution of an AM process, so a full understanding of all the heat transfer mechanisms is extremely important. Convective fluxes within the molten pool are caused by thermal and concentration gradients and their influence on the local temperature field is generally much higher than that of the sole conduction [11]. Some authors completely neglect this aspect, assuming a low influence of the fluid-dynamic behaviour for the chosen set of parameters (e.g. for high scanning speeds); others include the macroscopic effect of the enhanced thermal diffusion by locally adjusting some thermal properties [12]. This kind of approach is indeed incomplete: the two physics, heat exchange and fluid-dynamics, interact between each other and neglecting this aspect can lead to an unacceptable approximation.

Thermo-fluid dynamics (TFD) models face the resolution of the problem in a more rigorous and quantitative way. Generally, for the sake of simplicity, the liquid metal is considered to be an incompressible Newtonian fluid and its flux within the molten pool is assumed to be laminar [11, 13]. This last hypothesis might be too strict and reduce the model accuracy: for this reason, some researchers [14, 15] implemented a turbulence model assigning effective conductivity and viscosity to the system. Regardless of the initial hypotheses, the two Navier-Stokes continuity and momentum conservation equations are solved at every iteration. Despite the generally good results reported by researchers, the implementation of a TFD simulation has not been considered in the present paper because of the additional numerical complexity given by the implementation of the Navier-Stokes equations, which is only useful to study the metal molten pool dynamics and not to simulate the complete process.

To simulate the building of bigger geometries, it is necessary to drastically reduce the size of the problem. Two different techniques have been implemented:

- **Inherent Strain (IS) Method**: this method consists in simulating the thermal stress build up at component scale by using a residual plastic strain (inherent strain) tensor which is activated in the individual hatching regions of a macro-scale mechanical model in a layer-by-layer fashion. This technique was originally developed to simulate welding processes and it has been adapted and modified for PBF simulation applications [16, 17, 18].

- **Equivalent Scanning Method**: a representative surface heat flux or body heat flux is applied to a target volume (e.g. hatching volume) or an entire layer for an arbitrary time period. The magnitude of the heat fluxes and the application time depend on the machine specific laser power and scanning speed [19, 20].

To scale down the problem, both of these two approaches simulate the building of bigger parts adding macro-layers, which represent a group of real layers. Despite the several simplifications, the numerical results of these simulations seem to show a good correlation with the experimental measurements.

Keller *et al.* [16] implemented the IS method using a multi-scale approach. A first, thermo-mechanical model was developed to simulate the scanning of a hatching-scale region and to determine the inherent strain tensor components. The obtained IS values were then activated in the mechanical simulation of a real component for fast stress/strain prediction. The numerically computed residual distortion shows a remarkably good agreement with the experimental measurements.

Alvarez *et al.* [17] studied the influence of the macro-layer size on prediction accuracy of their IS based macro-scale mechanical model. This allowed them to find the minimum required number of layers needed to approximate the experimentally measured distortion. However, inherent strain coefficients (via thermal expansion coefficients setting) were set up arbitrarily as no information is given regarding their determination. Li *et al.* [18], similarly to Keller, followed a multi-scale approach to determine eigenstrain values and experimentally validated the output of their macro-scale model. Despite the good final results, the two thermal and thermo-mechanical simulations developed in this study were set up using temperature independent

material properties, which commonly leads to inaccurate predictions. Moreover, the results of the two intermediate simulations were not openly discussed and no detail was given on how the IS values were extracted.

In addition to these research papers, it is worth to notice that most of the new commercial AM simulation software that are being released in beta-version in these months implement the IS technique. Among others, there are:

- Simufact

- Amphyon

- GeonX

but a knowledge gap is evident as only a few studies deal with this method compared to the large number of papers that describe other simulation solutions. For this reason, this work is focused on the implementation and on the application of the inherent strain method to fully understand its capabilities and limitations. The details about this technique are thoroughly described and discussed in Section 3.

3. Proposed Solution

To enable a practical usage of a FEM based method for AM process simulation, calculation times and model complexity must be kept to a minimum.

A different approach is necessary to solve the problem. This is why a few researchers have tried to reduce the size of the simulation applying different techniques and simplifications (cfr. Section 2). In this section, the models based on the new IS method-based multi-scale approach proposed by Keller and Ploshikhin [16] are described and developed using Abaqus FEA.

This new technique is used to predict the stress state and residual deformation of the real part in a fraction of the time required by a complete thermo-mechanical analysis. It is based on the inherent strain (or eigenstrain) theory: the term was first introduced by Ueda in 1975 [21] to refer to the sum of all the incompatible internal permanent strains induced by inhomogeneous inelastic deformation, temperature gradients, or phase transformations that cause residual stresses after a welding process.

Based on the concept of eigenstrain, Mura [22] developed a mathematical framework for the determination of the residual stresses corresponding to a given eigenstrain distribution in case of an infinite three-dimensional body. However, it was Ueda himself who presented, between 1975 and 1994, a series of papers in which he applied the inherent strain method to finite element models. This method consists in the activation of experimentally measured or numerically computed eigenstrains within a simple finite element mechanical model to evaluate the welding residual stress and deformation. Specifically, for a simple elastic FE model, the relation of the inherent strain $\underline{\varepsilon}^*$ with elastic strains $\underline{\varepsilon}^{el}$ or stress $\underline{\sigma}$ produced by $\underline{\varepsilon}^{el}$ at

an arbitrary point of a three-dimensional body can be expressed by the following elastic response equations:

$$\underline{f} = \int_V \mathbf{B}^T \mathbf{D} \, \underline{\varepsilon}^* \, dV \qquad (1)$$

$$\underline{u} = \mathbf{K}^{-1} \, \underline{f} \qquad (2)$$

$$\underline{\varepsilon}^{tot} = \mathbf{B} \, \underline{u} \qquad (3)$$

$$\underline{\varepsilon}^{el} = \underline{\varepsilon}^{tot} - \underline{\varepsilon}^* \qquad (4)$$

$$\underline{\sigma} = \mathbf{D} \, \underline{\varepsilon}^{el} \qquad (5)$$

where

$\mathbf{B}$ = strain-displacement matrix
$\mathbf{D}$ = stress-strain matrix
$\mathbf{K}$ = stiffness matrix

To experimentally measure the inherent strains either X-ray/neutron diffractometric or extensometric measurements must be carried out. This experimental measurements based procedure is the one followed in a large number of papers about inherent strain method: once the welding is performed, the residual stress/strain state is measured along the weld at different distances near the bead. Arbitrary shape functions are fitted on the experimental values to reconstruct the inherent strain state as a function of spatial coordinates. The experimentally estimated eigenstrains are then activated in the macro-scale mechanical model for final stress/deformation prediction [21, 23].

On the other hand, for the numerically computed inherent strains a short welding path is simulated with a coupled thermo-mechanical analysis to directly find the eigenstrain components.

This sort of numerical "submodelling" approach is the one followed in [16]. The work is based on the consideration that the complete part is generated by a build-up of micro-welding processes and that each micro-weld seam experiences an identical or comparable thermo-mechanical history. This assumption is used to reduce the size of the problem, setting up a meso-scale nonlinear thermo-mechanical analysis only to simulate the scanning on a small hatching region. The hatching region is in fact a small block, with a constant temperature history during the scanning, which is replicated several times for every layer and within each layer to build up the desired part.

The numerically computed strains are then applied as inherent strain in a macro-scale elasto-plastic FE model to predict residual stresses and deformations of the real part.

Compared to the complex thermo-mechanical analysis, only a very short computational time is needed to complete the simulation even for large and complex structures. The inherent strain FE analysis is also simpler to set up since temperature dependent material properties are not needed: it only uses the material constitutive law and its Poisson's ratio at ambient temperature.

In the following two sections, the two models and their implementation are described while the results

and the performance of this method are discussed in Section 4. For model validation, the results of the experimental campaign described in Appendix A were employed; therefore, the characteristics of the Renishaw AM250 SLM machine and of the maraging 18Ni300 material used for the experiment were studied and implemented in the model. In particular, the 18Ni300 material properties are reported in Table 1 and Fig. 2, while the process parameters used in the experimental work are reported in Table 2.

Table 1: Maraging steel (18Ni300) properties

Property	Unit	Value
Solidus temperature, T_S	[K]	1698
Liquidus temperature, T_L	[K]	1728
Latent heat of fusion, L_f	[J·(kgK)$^{-1}$]	242500
Poisson's ratio, ν	[-]	0.31

Table 2: Default building process parameters for 18Ni300 steel

Parameter	Unit	Value
Power, P	[W]	200
Exposure time, t_{exp}	[µs]	80
Focus distance, f	[mm]	0
Scan strategy		Hatching
Point distance, d_p	[µm]	65
Hatch distance, d_h	[µm]	80
Layer thickness, LT	[µm]	40

3.1. Meso-Scale Submodel

A small hatching-scale, two-layers, uncoupled thermo-mechanical simulation is developed using Abaqus FEA. The geometry is shown in Fig. 3: it is a 5×5 mm, 80 µm thick powder island deposited over a 18Ni300, 2 mm thick substrate that represents the previously built layers.

A larger shape was modelled in order to have conduction as heat transfer mode also on the sides of the scanned island, instead of assigning unrealistic boundary conditions directly on the sides of the representative region [6, 24, 25].

In this analysis, the metallic powder in the simulation space is modelled as a continuum. Powder bed characteristics strongly depend on its discrete nature but modelling each single grain in a macro/mesoscopic analysis would be computationally infeasible. In order to approximate the real powder bed behaviour, equivalent material properties are assigned to the powder. Only density and conductivity are affected by the powder discrete nature, the other properties are the ones of bulk material [26, 27]. The relative density ρ_{rel} of the powder bed at ambient temperature was computed from the ratio between the apparent density

of the powder, ρ_{powder}, and the density of the solid 18Ni300 material, ρ_{bulk}:

$$\rho_{rel} = \frac{\rho_{powder}}{\rho_{bulk}} = \frac{4400}{7425} \approx 59.26\% \qquad (6)$$

This value is considered constant for all the temperatures up to liquidus temperature, T_L, so:

$$\rho_{powder}(T) = \rho_{rel} \cdot \rho_{bulk}(T) \qquad (7)$$

The conductivity of the powder bed is computed from the Tolochko model [28], which assumes that each powder grain is approximately spherical, like for gas-atomized powders which are commonly used in AM. The model considers the total equivalent conduction coefficient (k_{eq}) in a porous media as the sum of different contributions: radiative thermal conduction through the pores (k_{rad}) and contact thermal conduction between the particles (k_{cond}):

$$k_{eq} = k_{rad} + k_{cond} \qquad (8)$$

where

$$k_{rad} = \frac{16}{3} l_{ph} \sigma_{SB} T^3 \qquad (9)$$

$$k_{cond} = \Lambda k_0 r_c \qquad (10)$$

where l_{ph} is the mean photon path, σ_{SB} is the Stefan-Boltzmann constant, T is the temperature, Λ is the normalized contact conductivity, k_0 is the bulk conductivity and r_c is the contact size ratio $\frac{b}{r}$ (Fig. 4), which is set to 0.2 [11].

The mean photon path between the powder particles l_{ph} is approximately the pore size and it is estimated to be equal to the solid powder mean particle size: 30.5 µm [11]. The normalized contact conductivity Λ values are reported on Table 3 for four different regular packing structures.

Table 3: Normalized contact conductivity of regular structures [28]

Packing structure	ρ_{rel}	n	Λ
Diamond	34%	4	0.433
Simple cubic (SC)	52.4%	6	1
Body-centered cubic (BCC)	68%	8	1.732
Face-centered cubic (FCC)	74%	12	2.828

Gusarov et al. [29] report a simple formula (eq. (11)) to find the Λ value for a random packing structure. Assuming a mean coordination number n equal to 7 and using the previously calculated powder bed packing density from eq. (6), the normalized contact conductivity can be easily computed:

$$\Lambda = \frac{n \rho_{rel}}{\pi} = \frac{7 \cdot 59.26\%}{\pi} = 1.3204 \qquad (11)$$

According to literature, all the other thermal properties (specific heat, latent heat) are treated as material
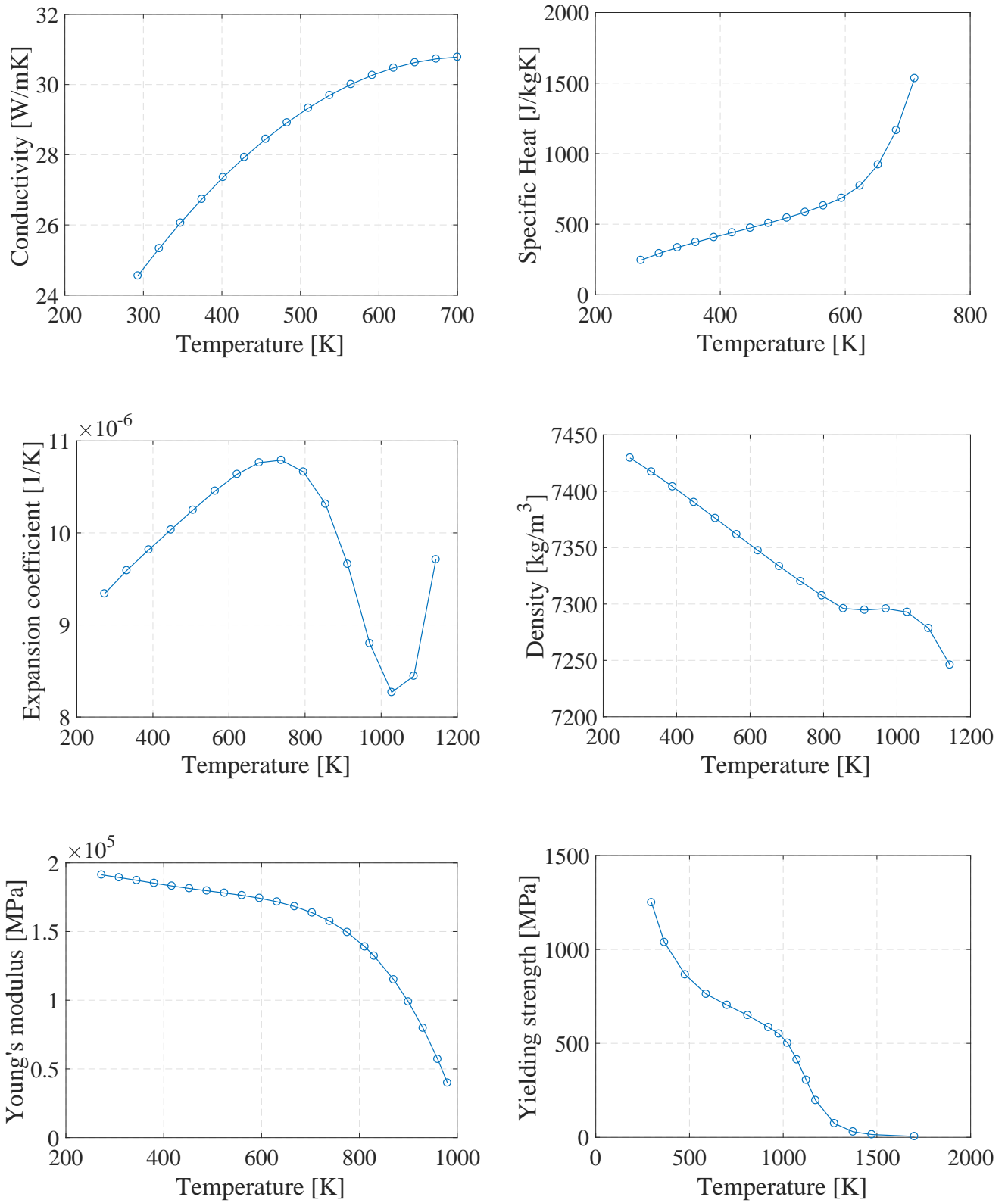
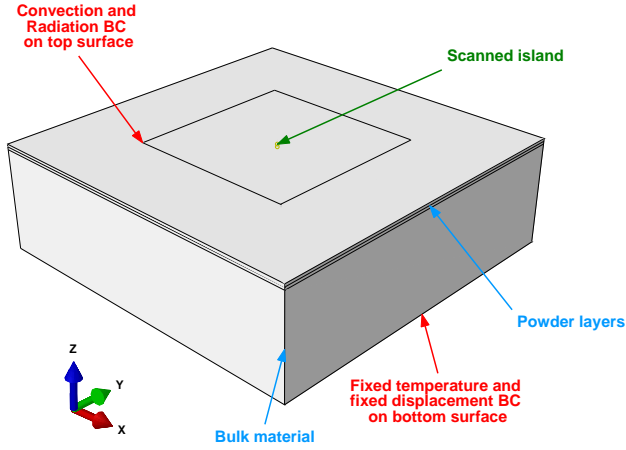**Figure 2:** Temperature dependent 18Ni300 properties
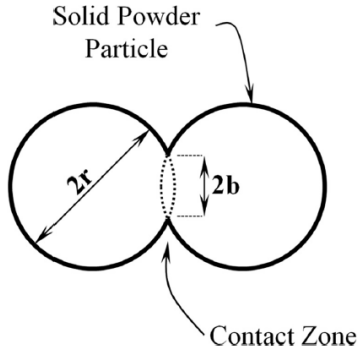
Figure 3: Meso-scale submodel geometry

Figure 4: Contact zone between two particles [11]

dependent only, so they do not change with its aggregation state [26, 27].

The powder layer is scanned by a pulsating Gaussian surface heat flux which follows the meandering pattern shown in Fig. 6a; a DFLUX subroutine was written for this purpose using the scanning properties reported in Table 2.

The phase change of powder material is programmed using the USDFLD subroutine to define a temperature dependent state variable. The phase change in this model affects both thermal and mechanical properties. At powder state, the material is set to have a null expansion coefficient and a small elastic modulus (it is not set to zero only to avoid any numerical instability): this is because the powder is loose and its aggregation state makes it irrelevant for the stress and strain state computation of the hatching region. Once the powder temperature exceeds T_L, its thermo-mechanical properties are switched to the ones of solid 18Ni300 (Fig. 2).

Fixed temperature boundary condition (BC) is set at the bottom of the substrate, while forced/natural convection and radiation boundary conditions are applied on the top surface.

In the first step of the thermal analysis, the second layer is deactivated and the surface heat flux scans the hatching region of the first layer following the me-

andering pattern. The argon recirculation pump is on when the laser scans the powder layer, therefore forced convection coefficient ($h_f = 42.86$ [W·(m²K)⁻¹]) is imposed using the FILM subroutine. Once the beam finishes scanning the region, the second layer is reactivated, simulating the new layer deposition; in this step, the recirculation pump is off and natural convection ($h_n = 8.15$ [W·(m²K)⁻¹]) is imposed on the top surface of the model. Forced convection is then reactivated together with the laser scan to build the second layer. A final steady-state cooling step with natural convection closes the analysis simulating the end of the building process. Details about the convection coefficients calculations are reported in Appendix B.

The temperature history obtained from the thermal analysis is loaded as input of the mechanical analysis. The FE mesh is kept the same to avoid incompatibility between the models and the geometry is constrained with a fixed displacement boundary condition at the bottom of the substrate.

At the end of the simulation, the final plastic strain state of the scanned island is obtained (Fig. 5). The distribution of plastic strain seems to be fairly regular across the layer for all of its 6 components. In order to be applied to the macro-scale model, an equivalent, mean inherent strain tensor must be extracted from the scanned region. A weighted average (Eq. (12)) was computed for each of the 6 strains using their centroid values and the element volume as weight:

$$\bar{\varepsilon}_{ij}^* = \frac{\sum_k^{N_{el}} V_k \cdot \varepsilon_{ij,k}^*}{\sum_k^{N_{el}} V_k} \tag{12}$$

where N_{el} is the total number of elements in the hatching region, V_k is the k-th element volume, and $\varepsilon_{ij,k}^*$ is the ij component of the plastic strain tensor at the centroid of the k-th element. The values computed are reported on Table 4.

Table 4: Average plastic strain tensor components

Strain component	Value
Normal x, $\bar{\varepsilon}_{11}^*$	2.05×10^{-3}
Normal y, $\bar{\varepsilon}_{22}^*$	0.30×10^{-3}
Normal z, $\bar{\varepsilon}_{33}^*$	-2.35×10^{-3}
Shear xy, $\bar{\varepsilon}_{12}^*$	-3.29×10^{-8}
Shear xz, $\bar{\varepsilon}_{13}^*$	-1.56×10^{-6}
Shear yz, $\bar{\varepsilon}_{23}^*$	4.45×10^{-5}

Normal strain components are roughly two orders of magnitude larger than the shear ones. This result is in agreement with what is reported in [16], where only the more relevant normal components have been considered for the macro-scale analysis.

3.2. Macro-Scale Model

The plastic strains determined in the hatching submodel are applied as inherent strains in the macro-scale model. The real part is sliced into macro-layers
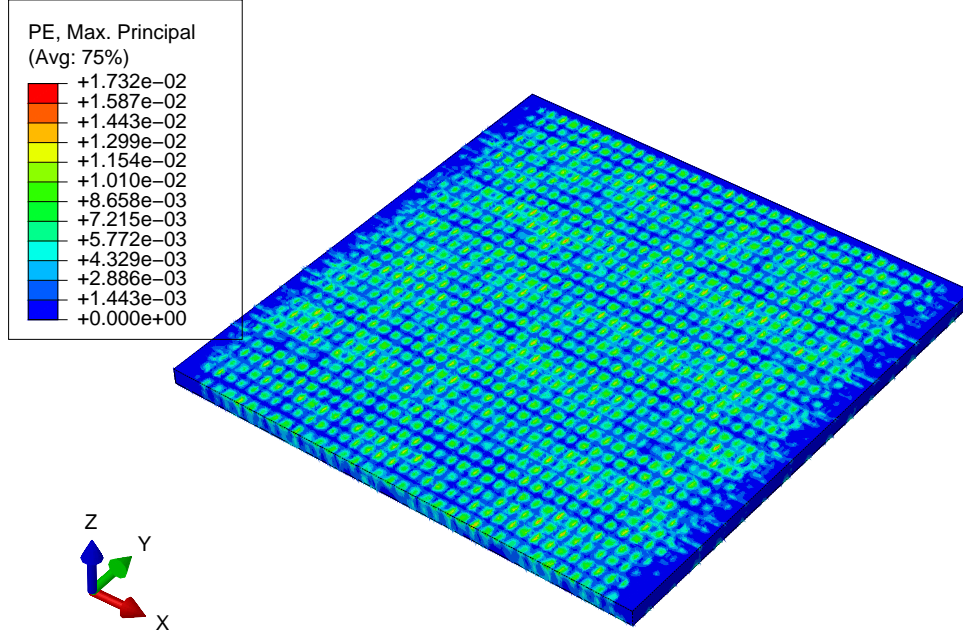
Figure 5: Hatching region plastic strain magnitude

that are sequentially activated with the corresponding eigenstrain values, simulating the layer build-up along the z-axis. The base plate of the PBF process is represented as a fixed displacement boundary condition at the bottom nodes of the manufactured part.

The strains computed with the submodel provide the fundamental strain components of each single "scanned island". By rotating this original eigenstrain tensor ε^*computed for Fig. 6a scanned island, every other orientation can be considered:

$$\varepsilon^*_{rot}(\vartheta) = \mathbf{R}\ \varepsilon^*\ \mathbf{R}^T \tag{13}$$

where $\mathbf{R}$ is the xy-plane rotation matrix, which is a function of the orientation angle ϑ of the scanned island.

$$\mathbf{R} = \begin{bmatrix} \cos(\vartheta) & \sin(\vartheta) & 0 \\ -\sin(\vartheta) & \cos(\vartheta) & 0 \\ 0 & 0 & 1 \end{bmatrix} \tag{14}$$

Virtually every hatching-based scanning strategy can be mapped within the macro-scale model by simply activating differently oriented eigenstrain tensors in different regions of the same layer. In fact, the orientation of the scanned islands can change across the same layer, therefore ϑ becomes a function of x and y position. This operation allows to determine the so-called "Mechanical Layer Equivalent" (MLE) for each generated layer, which will specifically depend on the applied scan strategy.

This macro-scale, inherent strain method-based FE model was developed using Abaqus FEA and it implements the following general characteristics:

- the material properties of 18Ni300 maraging steel at ambient temperature were approximated to
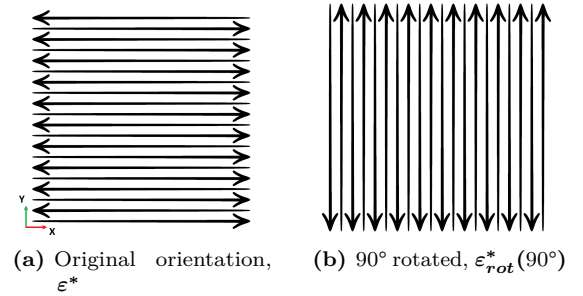

(a) Original orientation, ε^*

(b) 90° rotated, $\varepsilon^*_{rot}(90°)$

Figure 6: Example of differently oriented scanned islands with their corresponding strain tensor

have an elastic-perfectly plastic mechanical behaviour. The implemented properties are reported in Table 5 [30];

Table 5: 18Ni300 mechanical properties at T_{amb}

Material properties	Value
Young's modulus, E [MPa]	191000
Yielding strength, σ_y [MPa]	1250
Poisson's ratio, ν	0.31

- before the end of the analysis, after the stepwise activation of layers and inherent strains, the fixed displacement boundary condition is removed at the bottom of the model except for a small region where it is kept active to avoid stiffness matrix singularity. This operation simulates the part release from the base plate and allows to obtain the final residual stress distribution and deformation.

A simple thermo-mechanical analysis was set up to

implement the inherent strain method [23].

Anisotropic thermal expansion coefficients were added to the material properties: each coefficient is equal to its corresponding inherent strain (e.g. $\alpha_{11} = \varepsilon^*_{11}$). A unitary temperature change is then imposed and the equilibrium solution for residual stress is computed for each layer activation.

The orientation of the scanned islands is considered by changing the material orientation in the different regions of each layer, while the macro-layer addition is handled using the *Model Change* feature, which is set up to deactivate all the layers except for the first one and to sequentially add them during the analysis.

A detailed study on the characteristics and on the performance of these two models is presented in the following section.

4. Results and Validation

For model validation, the results of the experimental campaign described in Appendix A have been employed. The test specimen geometry is reported in Fig. 7. Two factors were analysed in the full factorial experimental campaign:

- 3 scanning strategies:

  1. meandering pattern in *x*-direction ("mx", Fig. 8a);
  2. meandering pattern in *y*-direction ("my", Fig. 8b);
  3. chessboard pattern ("chess", Fig. 8c);

- 2 upper thicknesses:

  1. nominal thickness, 2.2 mm;
  2. half of the nominal thickness, 1.1 mm;

for a total of 6 treatments replicated 4 times. The response variable analysed in this experimental campaign was the maximum displacement along the building direction after part detachment from the working plate. The same value will be extracted from the simulations for model validation.

4.1. Submodelling Performance

The average plastic strains computed with the meso-scale submodel of Section 3.1 provide the inherent strain tensor components and they are now activated in 6 different macro-scale mechanical models created to numerically reproduce the 6 treatments described at the beginning of this section. To test their capabilities in predicting the final deformation of the experimental specimens, the bending values obtained from the macro-scale numerical models are directly compared to the measured mean deformation of the 6 corresponding experimental treatments in Table 6. The treatments' mean 95% confidence interval is plotted together with the numerical predictions in Fig. 10.

Table 6: Submodelling performance

Scan strategy	Upper thickness	Bending [μm]	
		Exp. mean	Abaqus
mx	1.1 mm	-568.6	-576.9
	2.2 mm	228.9	-453.8
my	1.1 mm	-1294.3	-294.5
	2.2 mm	-315.4	-187.7
chess	1.1 mm	-1235.7	-408.5
	2.2 mm	-49.8	-307.4

All the 6 macro-scale models, when the computed inherent strains are activated, show a negative deformation value. This means that, with the computed inherent strain tensor, the simulated AM parts bend in the same direction of almost all the experimental treatments. In fact, only for one treatment (scan strategy: *mx*, upper thickness: 2.2 mm) the numerical model of the part did not deform in the same direction.

By comparing the results, the model of 1.1 mm geometry and *mx* scan strategy treatment seems to predict extremely well the experimental final deformation after the activation of the submodel's IS tensor. Even the residual deformation computed for the 2.2 mm geometry and *my* scan strategy treatment falls just slightly outside of the 95% mean confidence interval.

All the other numerically computed bending values are extremely far from the experimental observations. In addition, the only two treatments that show a good correlation with the numerical models do not seem to give any indication about an experimental subgroup for which the computed eigenstrain tensor is valid, since they belong to different scanning strategies and geometries.

In conclusion, under the assumption that the inherent strain method, as applied in [16], can actually predict the residual stress/deformation state, this poor performance can only indicate that the IS values obtained from the thermo-mechanical simulation of the scanned island of Section 3 are not accurate. A new approach to improve the performance of eigenstrain method-based AM simulation is presented in the following section.

4.2. Calibration

According to the framework presented in section 3 and followed in section 4.1, the two developed models are made to be used together. The solution of the first meso-scale thermo-mechanical model provides the eigenstrain tensor that is activated in the macro-scale mechanical simulation. This method allows to leave out any kind of experimental work, relying completely on the results of the FE analysis. Despite being extremely convenient, this approach can hide some flaws.
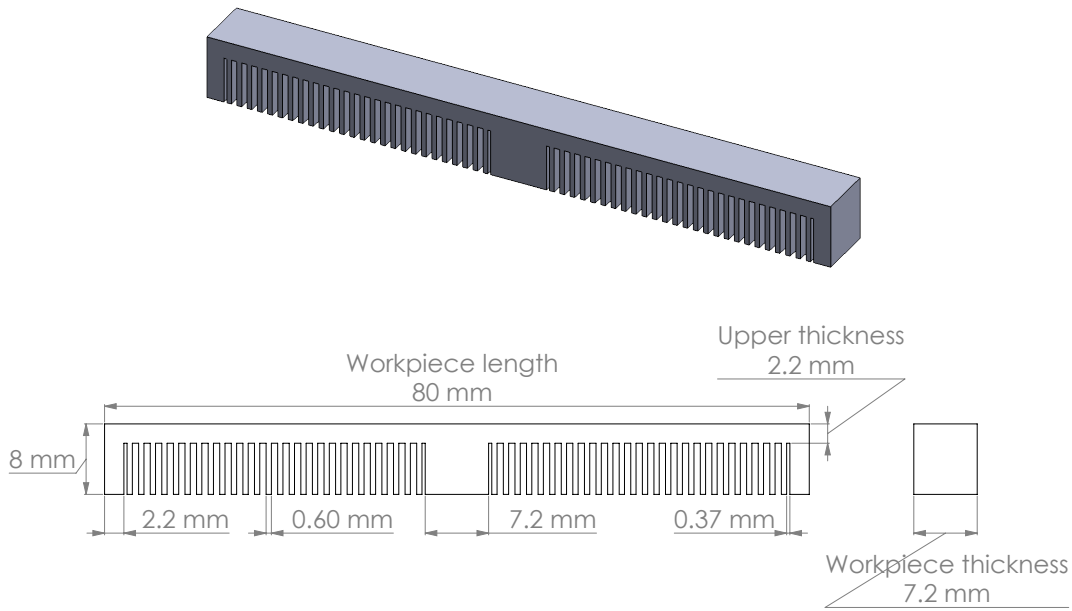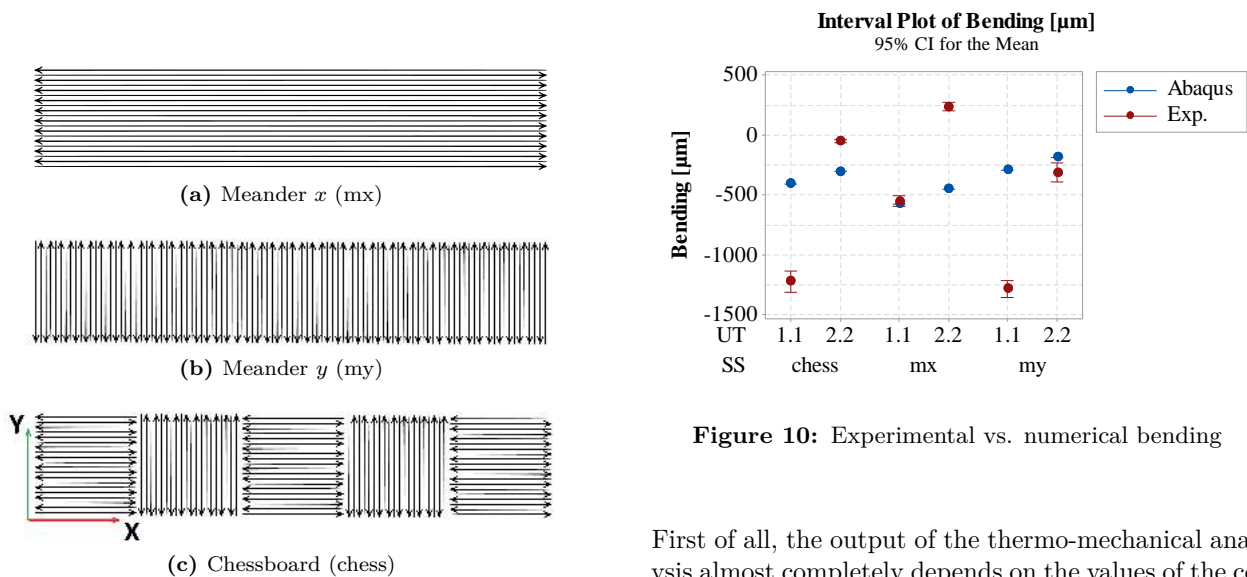
Figure 7: Cantilever geometry

(a) Meander x (mx)

(b) Meander y (my)

(c) Chessboard (chess)

Figure 8: Experimental scanning strategies

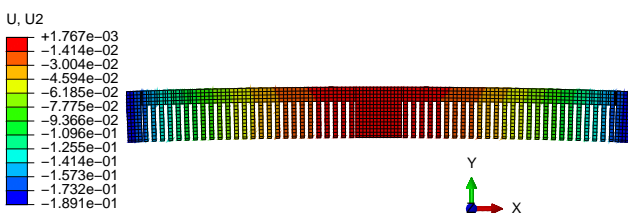**Figure 10:** Experimental vs. numerical bending

Figure 9: Example of numerical bending computation

First of all, the output of the thermo-mechanical analysis almost completely depends on the values of the coefficients used to define the material properties. Given the wide temperature range covered during the process and the simulation, most of the properties must be defined as a function of temperature: this makes everything more difficult because the coefficients are not always available in literature and should be experimentally evaluated, taking into account the fact that material thermo-mechanical characterization can be extremely costly and critical, especially at high temperatures.

Nevertheless, even if the material properties are available in literature, the data might not perfectly fit the material in use.

Also powder properties in these simulations are crucial and they are usually derived from models that are based on strong simplifying hypotheses.

A few researchers decided to apply calibration on their thermo-mechanical simulations with respect to a few parameters (e.g. absorption, laser power distri-

bution) [4, 16, 31], but, probably due to the computational effort, a complete and exhaustive work on the uncertainty of all the parameters and on its propagation on the final results has not yet been made to this date.

A hybrid, experimental-numerical approach is proposed here to avoid all the problems related to the uncertainty of the parameters of the thermo-mechanical simulation. Instead of solving the meso-scale model to get the values of the inherent strain tensor, with this approach the values are obtained by calibrating the large-scale mechanical analysis on the experimental data.

Compared to the thermo-mechanical model, the macro-scale model requires only ambient temperature material mechanical properties, which are much easier to find in literature or to experimentally measure with a much lower uncertainty.

Keller, in his first work on the eigenstrain method [16], reported that all the off-diagonal terms of the inherent strain tensor in the scanned island region tended to 0. This was also confirmed by the results obtained in 3.1. Furthermore, a sensitivity analysis carried out on the macro-scale model showed that the eigenstrain component in the building direction ε_{zz}^* has no influence on the residual stress state. Therefore, only the normal strain components on the layer plane (ε_{xx}^* and ε_{yy}^*) are assumed have a significant effect on the final bending value.

4.2.1. Regression-based Optimization

The response of the model, in terms of maximum displacement, for different sets of layer-plane inherent strains was computed and a regression equation was fitted. This operation was carried out for each of the 6 treatments models and, in each case, bending was found to be a linear function of x and y strains:

$$\hat{f}_i = a_i \cdot \varepsilon_{xx}^* + b_i \cdot \varepsilon_{yy}^* + c_i \quad (15)$$

where, for each i-th treatment, $\hat{f}_i$ is the estimated numerically computed residual bending value, and a_i, b_i and c_i are the three regression estimated coefficients.

Therefore, optimal inherent strains could be computed by solving a simple system of linear equations. This procedure represents indeed an approximation of the actual solution but it allowed to carry out a much broader investigation on the calibration performance, because regression-based parameters optimization only requires a fraction of the time needed for software-based calibration.

In the next section, the post calibration performance of the Abaqus FEA macro-model for all possible calibration subsets is reported and the stress/deformation prediction capabilities of the eigenstrain method applied to a PBF process is discussed.

In section 4.2.3, a more detailed study with software-based eigenstrain optimization will be presented but it will be focused only on the most significant calibration strategies.
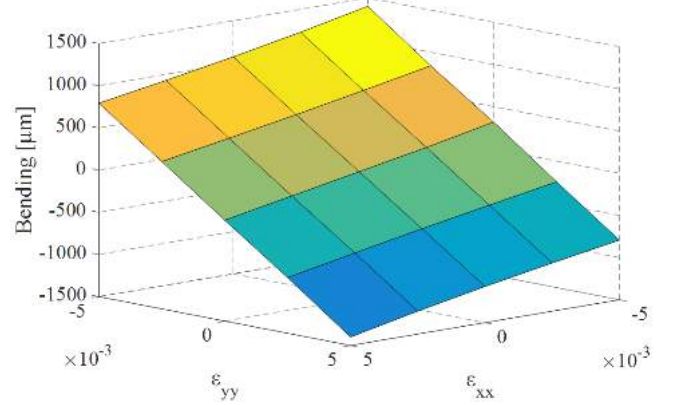
Figure 11: Example of model response for different IS combinations

4.2.2. Cross Validation

Let A be the set of the experimental campaign specimens; S_{cal} is the arbitrary calibration/training subset and $S_{cal} \subset A$. The performance of the calibration is evaluated computing the *Root Mean Square Error* (RMSE) on the so-called validation subset, which is defined as $S_{val} = S_{cal}^{\complement} \cap A$, and on the calibration subset (Eqs. (16) and (17)):

$$\text{RMSE}_{val} = \sqrt{\sum_k \frac{(\hat{f}_k(\varepsilon_{xx,cal}^*, \varepsilon_{yy,cal}^*) - f_k)^2}{|S_{val}|}},$$
$$\forall k \in S_{val} \quad (16)$$

$$\text{RMSE}_{cal} = \sqrt{\sum_k \frac{(\hat{f}_k(\varepsilon_{xx,cal}^*, \varepsilon_{yy,cal}^*) - f_k)^2}{|S_{cal}|}},$$
$$\forall k \in S_{cal} \quad (17)$$

where f_k and $\hat{f}_k(\varepsilon_{xx,cal}^*, \varepsilon_{yy,cal}^*)$ are respectively the measured and the numerical residual bending of the k-th specimen; $\varepsilon_{xx,cal}^*$ and $\varepsilon_{yy,cal}^*$ are the two eigenstrains obtained after model calibration on the training set S_{cal}.

All the possible calibration strategies have been investigated. For this purpose, the complete set of 24 measurements was split into the 6 experimental treatments. The calibration subsets analysed in this section are composed by every possible combination of the 6 treatments. Therefore, each experimental treatment is a factor of an approximately 2^k factorial plan with $k = 6$ and a total of 62 treatments, which is equal to the 64 combinations of the 6 treatments minus the $S_{cal} = \emptyset$ and the $S_{cal} = A$ treatments. The studied calibration subsets are composed by:

- 6 single treatments;
- 15 combinations of 2 treatments;
- 20 combinations of 3 treatments;
- 15 combinations of 4 treatments;

- 6 combinations of 5 treatments.

To clearly identify each treatment and simplify data handling, a number from 1 to 6 was assigned to each experimental treatment. The 6 treatments/factors names are reported in Table 7.

Table 7: Treatment/factors coding

Upper	Scan strategy		
thickness	mx	my	chess
1.1 mm	1	2	3
2.2 mm	4	5	6

For simplicity, the two RMSEs were plotted against another factor named *Strategy* whose value describes the combination of the treatments used for calibration (e.g. "126" is a calibration subset composed by the *mx* and *my* scan strategy of upper thickness 1.1 mm and the *chess* scan strategy of 2.2 mm). Figure 12 clearly shows that the worst performance on the validation subset is obtained when the models are calibrated combining the 2 treatments with the same scan strategy (*Strategy*: 14, 25 and 36 show all a $\text{RMSE}_{val} > 4000$ µm), while all the other calibration subsets seem to perform similarly ($\text{RMSE}_{val} = [500; 1000]$ µm). From Fig. 12 it is also possible to notice that when the model is calibrated on less than three treatments, the calibration procedure finds inherent strain values that fit the model very well on the experimental observations ($\text{RMSE}_{cal} < 50$ µm).

The model seems to fit fairly well also on the 123 and 456 calibration subsets, which are the two separate geometries calibration subsets, but their corresponding validation RMSEs are above 700 microns. This behaviour seems to point out some sort of underlying incompatibility between the calibrations of the two geometries. In fact, increasing the size of the calibration subset by mixing treatments coming from different geometries slightly improves the performance on validation but makes drastically increase the calibration RMSE. This confirms the fact that the models of the two geometries do not fit well on the same IS tensor, thus compromising the IS global validity on which the method is founded: in fact, the IS should be dependent only on material and process parameters and not on the geometry of the built component. The optimal IS tensor found for these strategies is only a compromise tensor whose activation in the macro-scale model produces bad results on all the treatments, making it a useless tool for prediction.

To summarize, it was observed that, for some conditions, calibrated models produce very good results within the calibration region but they all fail in predicting the bending of the treatments in the corresponding validation region. It is generally very easy to find a suitable set of residual strains that fit the calibration subset data, but this is not sufficient: only

by validating the results it is possible to determine the real capabilities of this approach.

According to the fundamental assumption of IS method [16], the inherent strain values only depend on the thermal history of the "scanned island" and should not be a function of macroscopic dimensional characteristics such as the upper thickness h. In fact, all the AM eigenstrain method-based simulations are founded on this hypothesis but, from the calibration strategies analysis, this claim of global validity of the eigenstrain tensor seems to fall short.

This hypothesis could either be wrong, and the validity of the method be compromised, or the thermal history experienced by the specimens of the two geometries during the building process is so different that it significantly influences the residual stress state. In fact, it must be noticed that the two geometries were built together on the same plate and, due to the difference in height, the building of the additional layers of the 2.2 mm specimens could have affected the final stress distribution.

Before drawing any conclusion, a more in-depth analysis on the separate geometries calibration strategies is carried out using the more accurate software-based parameters optimization.

4.2.3. Software-based Optimization

As reported in Section 4.2.1, the RMSE values analysed in the previous section were computed using regression models to find approximate eigenstrain values: this approach allowed to study a very large number of calibration strategies without relying completely on slow software-based parameters optimization. These results provided an interesting insight of the calibration performance, allowing to draw some general conclusions about the inherent strain method and to pick the best calibration subsets.

Nevertheless, relying completely on regression models only approximates the optimal solution: to achieve the maximum accuracy for eigenstrains estimation, an iterative parameters optimization based on the real results of the FEM model is the only possible solution but, since this approach is very computationally expensive, optimal eigenstrain values were computed only for the few, best performing calibration strategies.

The optimization procedure was implemented using the Abaqus built-in Python interpreter. The Broyden–Fletcher–Goldfarb–Shanno (BFGS) optimization algorithm [32] included in the SciPy library [33] was used to minimize the objective function (Eq. (18)) with respect to the two layer-plane inherent strains $(\varepsilon_{xx}^*, \varepsilon_{yy}^*)$:

$$\min_{\varepsilon_{xx}^*, \varepsilon_{yy}^*} \sum_i \sum_{j=1}^4 (\bar{f}_i(\varepsilon_{xx}^*, \varepsilon_{yy}^*) - f_{i,j})^2, \ \forall i \in S_{cal} \quad (18)$$

where $\bar{f}_i(\varepsilon_{xx}^*, \varepsilon_{yy}^*)$ is the numerically computed residual bending of the i-th treatment and $f_{i,j}$ is the de-
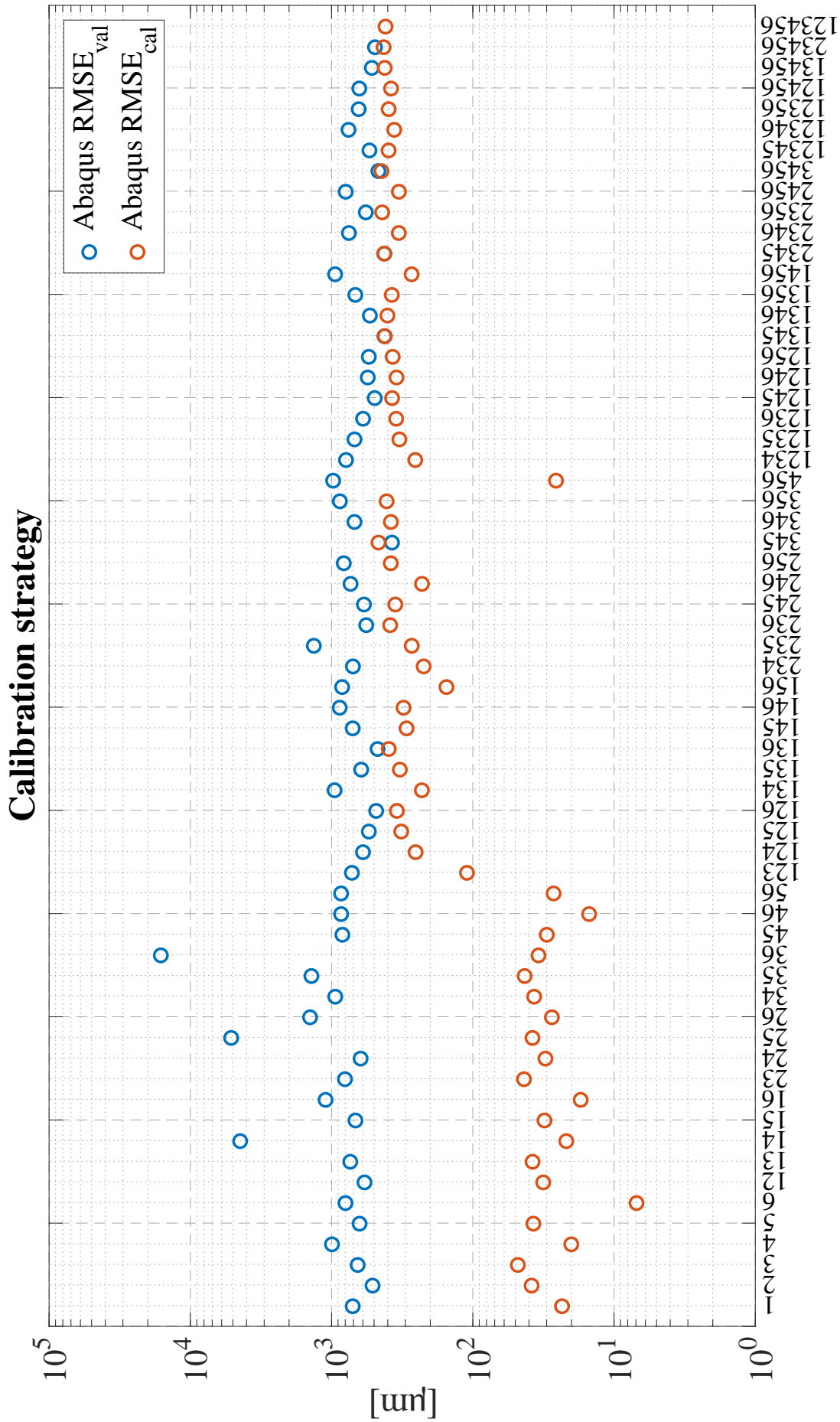
Figure 12: RMSE values for Abaqus

formation measured on the j-th replicate of the i-th treatment.

Among all the possible optimization algorithms (e.g. Nelder-Mead simplex, conjugate-gradient, genetic algorithm etc.), a quasi-Newton method, was chosen because the objective function is supposed to have only one absolute minimum, given the linear relation between the inherent strains and the residual bending found in Section 4.2.1. Therefore, Eq. (18) minimization does not require computationally heavy algorithms (e.g. genetic algorithm) which are more effective in presence of local minima. The regression-estimated shape of the generic objective function (Eq. (18)) is shown in Fig. 13.
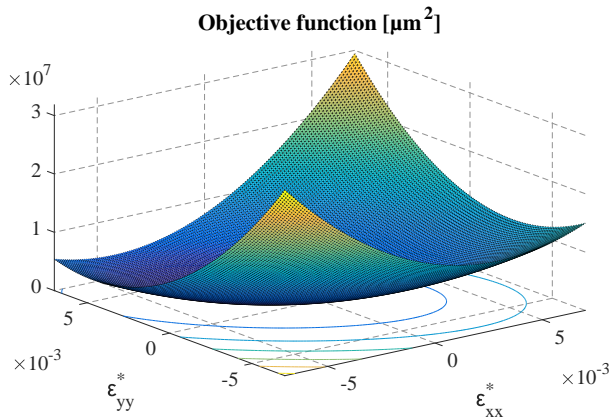
Figure 13: Regression-estimated objective function shape

Table 8 compares the optimal eigenstrain values computed from regression and from parameters optimization. A general linear model was fitted on these data to determine the influence on the computation of the optimal eigenstrains of the three factors:

- *Calibration Geometry*: 1.1 or 2.2 mm upper thickness;

- *Calibration Strategy*: mx+my, mx+chess or my+chess;

- *Calibration Method*: regression or software-based.

From the results of the ANOVA analysis (Table 9), it is clear that the optimization method does not influence the results, since the regression-estimated strains are very close to the ones obtained with optimization. This means that for fast parameter optimization, the regression approach in this case is very reliable: in fact, the parameter optimization of each strategy based on the BFGS algorithm required to run several analyses, thus resulting in 5-10 hours of computation time, while the regression approach only required to solve a simple system of linear equations (cfr. Section 4.2.1). However, since the implemented optimization procedure works directly on the software and since it is not sure that every geometry has the same linear relation between eigenstrains and residual bending, optimization algorithms are the most reliable solution, despite being more computationally expensive.

The two other factors, *Geometry* and *Strategy*, and their interaction significantly influence the optimal eigenstrains computation, in contrast with the fundamental principle of AM IS theory, according to which the eigenstrains should only be a function of the thermal history and nothing else. To further analyse this critical result, a pairwise comparison of these factors combinations was performed.

```
────────── Optimal IS Tukey ──────────


Comparisons for eps_x

Tukey Pairwise Comparisons:
Response = eps_x, Term = Geometry*Strategy

Grouping Information Using the Tukey Method
and 97.5% Confidence

Geometry*Strategy  N       Mean  Grouping
1 my+chess         2   0.0026980  A
1 mx+my            2   0.0002461      B
1 mx+chess         2  -0.0003598      B
2 mx+chess         2  -0.0015325          C
2 mx+my            2  -0.0016035          C
2 my+chess         2  -0.0020520          C

Means that do not share a letter are
significantly different.

%---------------------------------------------

Comparisons for eps_y

Tukey Pairwise Comparisons:
Response = eps_y, Term = Geometry*Strategy

Grouping Information Using the Tukey Method
and 97.5% Confidence

Geometry*Strategy  N       Mean   Grouping
1 mx+chess         2  0.0062810   A
1 mx+my            2  0.0047320       B
1 my+chess         2  0.0037705           C
2 my+chess         2  0.0020275               D
2 mx+my            2  0.0019025               D
2 mx+chess         2  0.0016190               D

Means that do not share a letter are
significantly different.
c@FancyVerbLineefferent.
```

The inherent strains of every calibration strategy of geometry 2 do not appear to be significantly different from each other but they are significantly different from the eigenstrains computed using the treatments of geometry 1. This kind of incompatibility between the calibrated results of the two geometries was already indirectly pointed out in the previous analysis and these results support this conclusion.

Moreover, this comparison allows to discover another problem: the strains computed for geometry 1 vary significantly depending on the chosen calibration strategy. This clearly highlights another critical behaviour of the IS model: the tension build-up of geometry 1 treatments does not seem to respect the "Mechanical Layer Equivalent" (MLE) principle, based on scan

Table 8: Regression vs. software-based optimal inherent strains

Geometry	Strategy	Method	ε^*_{xx}	ε^*_{yy}
1 (1.1 mm)	mx+my	Regression	2.360E-04	4.699E-03
		Software	2.561E-04	4.765E-03
	mx+chess	Regression	-3.741E-04	6.270E-03
		Software	-3.456E-04	6.292E-03
	my+chess	Regression	2.668E-03	3.754E-03
		Software	2.728E-03	3.787E-03
2 (2.2 mm)	mx+my	Regression	-1.610E-03	1.887E-03
		Software	-1.597E-03	1.918E-03
	mx+chess	Regression	-1.573E-03	1.754E-03
		Software	-1.492E-03	1.484E-03
	my+chess	Regression	-1.778E-03	1.934E-03
		Software	-2.326E-03	2.121E-03

Table 9: ANOVA table for ε^*_{xx} and ε^*_{yy} analyses

Source	DF	P-Value
Geometry	1	0.000
Strategy	2	0.000
Method	1	> 0.500
Geometry*Strategy	2	0.000
Error	5	
Total	11	

strategy dependent inherent strain tensor rotation, for residual stress state prediction.

The three couples of layer-plane eigenstrains computed for the two geometries are plotted in Fig. 14. From this graph it is possible to see that the optimal x and y-direction inherent strains estimated for the three strategies of geometry 2 fit in a much smaller region than the ones of geometry 1.
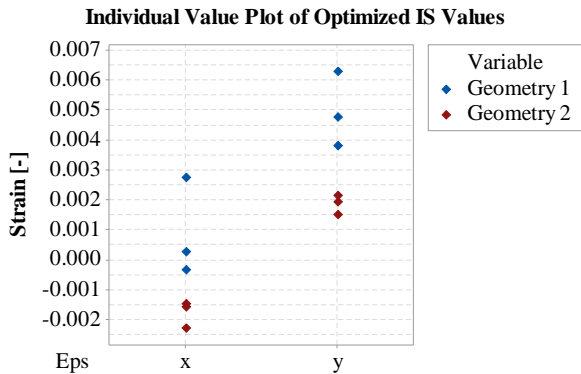

Figure 14: Software optimized IS values

The smaller dispersion of the optimal strains computed for the geometry 2 calibration strategies is the

reason of the better performance in prediction: in fact, regardless of the chosen 2-treatments calibration subset, the optimal set of strains does not vary significantly. This means that the residual stress and deformation state for all the treatments of this particular geometry is actually a function of the IS tensor orientation.

On the contrary, for geometry 1, the choice of the calibration subset affects much more the computation of optimal eigenstrain values, which result to be much more spread: this leads to a bigger error in prediction on the validation treatment because the optimal inherent strain values of the training subset are too different from the optimal values of the validation treatment.

The IS tensor compatibility found for geometry 2 treatments is not quite as valid for geometry 1 and the calibration of the two geometries are incompatible between each other because the optimal values computed for the treatments of one geometry are significantly different from the optimal values of the other one.

In Tables 10 and 11, the numerical bending values obtained for the 3 treatments of each geometry and for the 3 calibration subsets are reported next to the treatment's mean 95% confidence interval (CI) upper and lower bounds (UB, LB).

It is possible to notice that, while the calibrated subset values always fall in the confidence interval region, the predicted bending value for the validation treatment of each strategy, highlighted in the tables, is always outside.

The absolute difference between each numerical bending value and the corresponding treatment mean is reported in Table 12. A simple 1-sample t-test ($\alpha = 0.05$, null hypothesis H_0: $\mu_i = \bar{f}_{i,k}$) was also

Table 10: Residual bending [µm] computed with geometry 1 calibration strategies

Treatment	CI [95%]		Calibration strategy		
	LB	UB	mx+my	mx+chess	my+chess
1	-612.7	-524.5	-568.6	-568.6	-1124.0
2	-1381.6	-1207.0	-1294.3	-946.3	-1294.3
3	-1332.8	-1138.5	-1017.0	-1235.7	-1235.6

Table 11: Residual bending [µm] computed with geometry 2 calibration strategies

Treatment	CI [95%]		Calibration strategy		
	LB	UB	mx+my	mx+chess	my+chess
4	201.6	256.2	228.9	231.5	372.1
5	-377.7	-253.0	-315.4	-229.4	-316.7
6	-58.2	-41.4	-121.5	-53.7	-50.2

Table 12: Absolute difference between numerical prediction and treatment mean [µm], t-test p-value in brackets

Treatment	Calibration strategy		
	mx+my	mx+chess	my+chess
1	0 (*)	0 (*)	555.4 (0.0000)
2	0 (*)	348 (0.0011)	0 (*)
3	218.7 (0.0056)	0.05 (*)	0.05 (*)
4	0 (*)	2.6 (*)	143.2 (0.0005)
5	0 (*)	86 (0.0219)	1.3 (*)
6	71.7 (0.0001)	3.9 (*)	0.4 (*)

(*): p-value $\gg$ 0.05

carried out to statistically compare how far the predicted bending value $\bar{f}_{i,k}$ for each k-th strategy is from the experimental confidence interval of the i-th treatment. Before doing the t-test, the normality of the observations of all the 6 treatments was checked. In absolute terms, the calibration strategies perform better in prediction on geometry 2: for two out of three calibration strategies, the difference between the predicted bending and the validation treatment mean is less than 100 µm. However, despite the larger difference, from the comparison of the t-test p-values it is possible to see that some predicted values of geometry 1 validation treatments, due to their larger experimental variance, are less significantly different from the treatment mean with respect to the ones of geometry 2. Therefore, the results obtained from separate calibration of the two geometries are not very different in relative terms.

Furthermore, it is important to notice that calibration strongly depends on the experimental mean of the training subset's treatments: in fact, the model proved to be extremely flexible and the absolute difference between calibrated model bending and the treatment

mean tends to 0. To improve the calibration performance in prediction, it is crucial to correctly estimate the real treatment mean, therefore the number of replicates should be as high as possible.

In conclusion, inherent strain method worked very well for one particular condition, but the bad performance on the 1.1 mm geometry and the evident incompatibility between the calibrated eigenstrains of the two geometries still leave some questions open about the real capabilities of this method for AM simulation.

5. Conclusions and Future Developments

The in-depth analysis of the inherent strain method-based AM simulation carried out in this paper allowed to outline the strengths and the limitations of this new technique for fast prediction of the residual stress and deformation state.

The performance of two methods for inherent strain components determination were studied against the experimental results: (i) the original procedure, based on the coupled simulations technique described in

Section 3, and (ii) a new calibration-based approach, in which part of the experimental measurements are used to calibrate the output of the macro-scale IS model.

The prediction capabilities of this original "submodelling" procedure were found to be very poor and far from the extremely good results reported in [16]. This behaviour could be caused by the lack of accuracy of the thermo-mechanical simulation. The output of the AM macro-scale model completely relies on the computed eigenstrains of the meso-scale analysis but a big uncertainty lies behind the results of the thermo-mechanical simulation: this is because the determination of the analysis parameters and coefficients is extremely critical and the propagation of the possible input errors on the final results is not controllable. However, to clearly determine the accuracy of the thermo-mechanical simulation, future studies will focus on the experimental validation of the results of the submodel via residual stress characterization.

The calibration-based approach, which was originally created to improve the prediction results, allowed to examine in depth the IS method mechanisms. The results of this study evidenced a departure from the fundamental hypothesis on which the adapted IS method for AM simulation is based. It was discovered that when the calibration is carried out on a subset of treatments of one geometry, the model predicts fairly well the residual bending of the remaining treatment of the same geometry, confirming the validity of the eigenstrain tensor rotation method to find the "Mechanical Layer Equivalent" (MLE); on the other hand, this calibration strategy fails to predict the deformation of the other geometry. This kind of incompatibility is the reason of the poor global performance of most calibration strategies.

This discovery drew the attention on an unexpected behaviour of the IS model. According to the fundamental hypothesis of this method, the inherent strain values only depend on the thermal history of the "scanned island" and should not be a function of macroscopic dimensional characteristics such as the upper thickness h. Since both of the geometries were built using the same laser parameters they both should have experienced the same thermal history but they do not seem to respect the hypothesis of global validity of the inherent strain tensor.

The only possible reason of this incompatibility is that the thermal history experienced by the two geometries is significantly different. If this is true, simulation results could be influenced by the total scanning area size or by the job's variety of components. Therefore, to avoid affecting the simulation accuracy, serious productivity limitations, such as maximum total scanning area or job's components homogeneity, would be added to an already slow technology, thus reducing the appeal of the simulation approach.

As evidenced by the results reported in this paper, it is very easy to obtain a good fitting of the numerical results after model calibration. In fact, the IS based macro-scale model proved to be very flexible for fitting on specific subsets of experimental data, but it appeared very limited in providing real predictions. Real prediction capabilities can only be checked with proper validation because otherwise, if the model is not tested outside of the calibration region, the effectiveness of this method for AM simulation cannot be judged.

This paper tries to bridge the literature gap on this topic, featuring a complete validation procedure. However, additional experimental work will be required to definitively determine if this simulation, after model calibration, is really capable of predicting the residual stress state outside of the calibration region.

In future studies it would be important to build the calibration/validation geometries separately and on a less "crowded" work plate to avoid any thermal interactions:

- if the incompatibility problem is solved, further testing should be carried out to assess the model performance on completely different geometries, keeping into account that thermal interaction can strongly affect the residual deformation and thus the accuracy of the simulation;

- otherwise, the fundamental geometry-independence hypothesis of the inherent strain tensor would be rejected. In this case, the potential of this AM simulation technique would be compromised due to the geometry dependency and due to the limited prediction capabilities, since the model, after calibration, could only predict the residual stress state for different scan strategies of the same calibration geometry.

- to further investigate the geometry-independence hypothesis, a third calibration option will be tested: by using neutron diffraction [34, 35], the residual strains can be measured over a small representative region and then activated in the macro-scale simulation to test again its prediction capabilities. Neutron diffraction inspection will then be employed to assess any residual strain difference between parts built with the same process parameters but with different geometries.

Appendix A. Experimental Campaign and Results

For model validation, an experimental campaign was carried out. The test specimen was built com-

bining different process parameters and geometric characteristics (see Fig. 7): it is a small cantilever characterized by one principal post-process bending direction. The parts were built using a laser-based powder bed fusion machine, the Renishaw AM250 SLM system.

The FEA model implemented in this paper is capable of reproducing the residual stress state of the component; however, direct measurement techniques are very complex and limited in experimentally reconstructing the residual stress state of the real part. For this reason, indirect evaluations are very practical: complex residual stress states result in a global deformation of the part after release from the working plate. In addition, deformation measurements are non-destructive and much easier to carry out. Therefore, the response variable analysed in this experimental campaign was the maximum displacement along the building direction after part detachment from the working plate. In the following sections, the experimental campaign and the measuring technique is presented.

Appendix A.1. Experimental Campaign

A full factorial experimental campaign was created to analyse the influence of two factors on the residual stress state:

- 3 scanning strategies:

  1. meandering pattern in x-direction ("mx", Fig. 8a);
  2. meandering pattern in y-direction ("my", Fig. 8b);
  3. chessboard pattern ("chess", Fig. 8c);

- 2 upper thicknesses:

  1. nominal thickness, 2.2 mm;
  2. half of the nominal thickness, 1.1 mm;
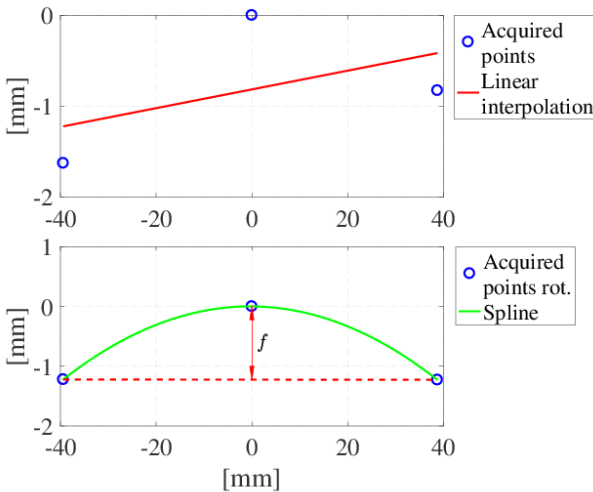
for a total of 6 treatments replicated 4 times.

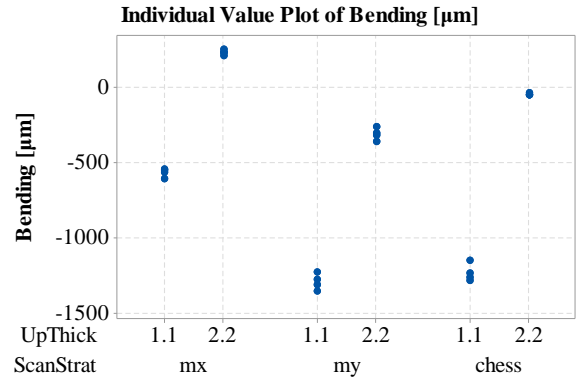

Figure A.15: Measuring technique

Figure A.16: Individual value plot of the residual bending

In addition to these two factors, also x and y position the specimen on the building plate are accounted in the ANOVA analysis to reduce the sources of variability in the model.

The manufactured specimens attached to the working plate are shown in Fig. A.17. To avoid influencing the specimen's residual stress distribution, a "gentle" release method, wire-cut EDM, was employed to remove the parts from the base plate. Any other technique could have affected the stress state and, as a consequence, the residual bending of the cantilever.

Appendix A.2. Measuring Technique and Results

The measurements on the released specimens are carried out using the Mitutoyo Quick Vision Pro, a CNC vision measuring machine with edge detection capabilities.

To measure the part residual bending, a 3 points set, 1 point on each end of the cantilever and 1 central point, has been acquired on the bottom of each specimen, where the cut was performed, because of the very low roughness. The central point is set to be the origin of the reference system and the other points are rotated around the origin by compensating the slope of the linear polynomial that interpolates all the points. Then, the mean vertical distance between the central point and the two extreme points is computed. Figure A.15 graphically displays the employed measuring technique on the points acquired on specimen 1.

Each bending measurement was replicated 5 times and its mean value was statistically analysed. For each of the 24 specimens, the computed mean bending is reported in Table A.13 next to the part number and treatment description.

The data are plotted in Fig. A.16. Mean, standard deviation and other descriptive statistics of the measured bending values for each treatment are reported in Table A.14.

Table A.13: Experimental plan results

Part	Upper thickness	Scan strategy	x-coord [mm]	y-coord [mm]	Bending [μm]
1	1.1 (-1)	my (0)	-0.991	-0.763	-1226.9
2	2.2 (1)	mx (-1)	-0.793	-0.863	250.7
3	1.1 (-1)	mx (-1)	-0.629	-1.000	-566.4
4	2.2 (1)	chess (1)	-0.268	-0.925	-52.0
5	1.1 (-1)	chess (1)	0.024	-0.925	-1237.7
6	2.2 (1)	mx (-1)	0.316	-0.925	228.1
7	1.1 (-1)	chess (1)	0.607	-0.925	-1149.6
8	2.2 (1)	my (0)	0.899	-0.925	-268.5
9	1.1 (-1)	my (0)	0.899	0.010	-1281.3
10	2.2 (1)	my (0)	0.607	-0.003	-310.0
11	1.1 (-1)	mx (-1)	0.188	-0.127	-607.9
12	2.2 (1)	my (0)	-0.011	-0.041	-319.0
13	1.1 (-1)	my (0)	-0.198	0.084	-1311.3
14	2.2 (1)	chess (1)	-0.559	0.012	-54.0
15	1.1 (-1)	chess (1)	-0.851	0.012	-1266.5
16	2.2 (1)	my (0)	-1.000	0.171	-364.0
17	1.1 (-1)	mx (-1)	1.000	0.729	-544.5
18	2.2 (1)	mx (-1)	0.771	0.814	228.0
19	1.1 (-1)	mx (-1)	0.607	0.948	-555.6
20	2.2 (1)	chess (1)	0.316	0.950	-51.2
21	1.1 (-1)	chess (1)	0.024	0.950	-1288.8
22	2.2 (1)	mx (-1)	-0.221	1.000	208.8
23	1.1 (-1)	my (0)	-0.559	0.948	-1357.7
24	2.2 (1)	chess (1)	-0.851	0.950	-42.1

Table A.14: Descriptive statistics of treatments

Scan strategy	Upper thickness	Descriptive stat. [μm]				
		Mean	StDev	Min	Max	Range
mx	1.1 mm	-568.59	27.67	-607.85	-544.50	63.36
	2.2 mm	228.88	17.13	208.76	250.65	41.89
my	1.1 mm	-1294.31	54.84	-1357.74	-1226.91	130.82
	2.2 mm	-315.36	39.17	-363.98	-268.50	95.47
chess	1.1 mm	-1235.68	61.06	-1288.85	-1149.64	139.21
	2.2 mm	-49.82	5.31	-54.03	-42.06	11.97

(a) Magics plate top view

(b) Built plate top view

(c) Lateral view
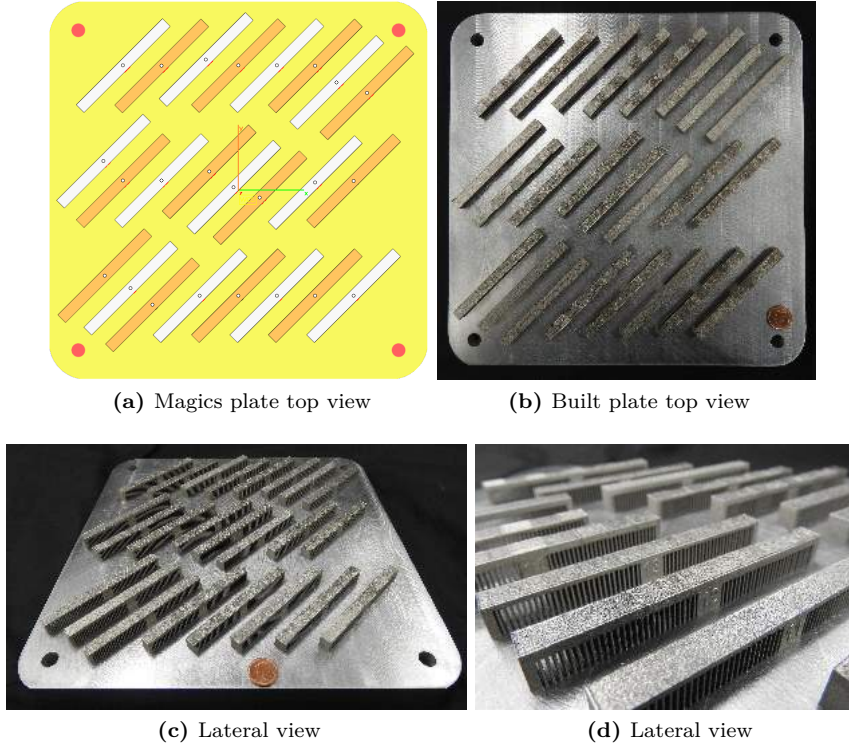
(d) Lateral view

Figure A.17: Job's digital model and built specimens

Appendix B. Auxiliary Models

The auxiliary models and the calculations made for complete process characterization are developed in this appendix section.

Appendix B.1. Convection Coefficients Computation

As reported in section 3, during the process, the working area is subjected to forced convection during the laser-on time and to natural convection during the other operations. For forced convection, the mean heat transfer coefficient h_f can be computed from the Nusselt number [36]:

$$Nu = \frac{h_f L}{k} = 0.664 \cdot Re^{1/2} \cdot Pr^{1/3} \qquad \text{if } Re < 5 \times 10^5 \tag{B.1}$$

The Reynolds and Prandtl numbers are defined as:

$$Re = \frac{\rho w L}{\mu} \tag{B.2}$$

$$Pr = \frac{c_p \mu}{k} \tag{B.3}$$

where ρ is the density, w is the velocity, μ is the dynamic viscosity, c_p is the specific heat and k is the conductivity of the argon flow. L is a characteristic length of the geometry analysed and, for the forced convection case, it is equal to the length of the plate (0.025 m). Table B.15 reports the physical properties of argon.

The value of Pr can be easily computed and it is equal to 0.6544. In order to compute Re, the velocity of the fluid flow must be found. The recirculation

Table B.15: Physical properties of Argon

Physical property	Unit	Value
Density ρ	[kg·m^{-3}]	1.784
Dyn. viscosity μ	[Pa·s]	2.23×10^{-5}
Specific heat c_p	[J·(kgK)$^{-1}$]	520
Conductivity k	[W·(mK)$^{-1}$]	0.01772
Molar mass MM	[g·(mol)$^{-1}$]	39.948
Adiabatic index γ	[-]	1.67

compressor installed on the machine is a SCL K03-MS MOR made by FPZ. The data-sheet reports a maximum flow of 73 m^3/h when rotating at 2900 rpm. During the laser-on time, the compressor rotates at 20 Hz, 1200 rpm. Therefore, the new maximum flow can be computed as:

$$Q_{1200rpm} = 74 \, \frac{1200}{2900} = 30.62 \, \frac{\text{m}^3}{\text{h}} \tag{B.4}$$

from the compressor affinity law.

Assuming a constant 0.03 friction factor, it is possible to find the operating point intersecting the system's and the compressor's curve (Fig. B.18).

The velocity of the fluid in the pipe ($\oslash$ 31.75 mm) is equal to 10.22 m/s and the Mach number is equal to 0.0316, far below the 0.3 threshold, so the fluid can be considered incompressible.

The gas is blown from 13 ($\oslash$ 12 mm) diffusers placed on the right of the building chamber. The argon
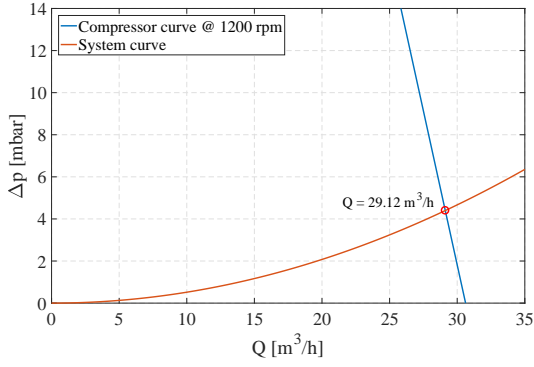
Figure B.18: Compressor's operating point

velocity at the outlet can be found from:

$$w = \frac{\dot{V}}{A_{tot}} = \frac{0.0081}{0.0015} = 5.5 \ \frac{\text{m}}{\text{s}} \qquad \text{(B.5)}$$

This value is used to compute Re from eq. (B.2), Nu from eq. (B.1) and h_f:

$$Re = 11003 \qquad \text{(B.6)}$$

$$Nu = 4.8832 \qquad \text{(B.7)}$$

$$h_f = \frac{kNu}{L} = 42.86 \ \frac{\text{W}}{\text{m}^2\text{K}} \qquad \text{(B.8)}$$

For the computation of the natural convection coefficient, the relation is [36]:

$$Nu = \frac{h_n L}{k} = 0.54 \cdot Ra^{1/4} \qquad \text{(B.9)}$$

where Ra is the Rayleigh number and the new characteristic length L is defined as the ratio between the area and the perimeter of the plate.
The Rayleigh number can be computed from the physical properties above, considering a mean ambient temperature T_{amb} equal to 300 K (from the building job's log file), a mean top surface temperature T_{surf} equal to 324 K (obtained from a simplified thermal simulation of the working plate) and approximating argon to a perfect gas.

$$Ra = \frac{g\beta(T_{surf} - T_{amb})L^3\rho^2 c_p}{\mu k} = 802.46 \quad \text{(B.10)}$$

where g is the gravity acceleration and β it the cubic expansion coefficient, which is $\approx T_{amb}^{-1}$. The natural convection coefficient h_n can be computed from eq. (B.9):

$$h_n = \frac{kNu}{L} = 8.15 \ \frac{\text{W}}{\text{m}^2\text{K}} \qquad \text{(B.11)}$$

Acronyms

ALE   Arbitrary Lagrangian-Eulerian

AM   Additive Manufacturing

BC   Boundary Condition

CFD   Computational Fluid Dynamics

DED   Direct Energy Deposition

FEM   Finite Element Method

FVM   Finite Volume Method

IS   Inherent Strain

LBM   Lattice Boltzmann Method

LC   Laser Cladding

PBF   Powder Bed Fusion

RMSE   Root Mean Square Error

SEBM   Selective Electron-Beam Melting

SLM   Selective Laser Melting

References

[1] Carolin Körner, Elham Attar, and Peter Heinl. Mesoscopic simulation of selective beam melting processes. *Journal of Materials Processing Technology*, 211(6):978–987, 2011.

[2] Carolin Körner, Andreas Bauereiß, and Elham Attar. Fundamental consolidation mechanisms during selective beam melting of powders. *Modelling and Simulation in Materials Science and Engineering*, 21(8):085011, 2013.

[3] Saad A. Khairallah and Andy Anderson. Mesoscopic simulation model of selective laser melting of stainless steel powder. *Journal of Materials Processing Technology*, 214(11):2627–2636, 2014.

[4] Saad A. Khairallah, Andrew T. Anderson, Alexander Rubenchik, and Wayne E. King. Laser powder-bed fusion additive manufacturing: Physics of complex melt flow and formation mechanisms of pores, spatter, and denudation zones. *Acta Materialia*, 108:36–45, 2016.

[5] Ninggang Shen and Kevin Chou. Simulations of thermomechanical characteristics in electron beam additive manufacturing. In *ASME 2012 International Mechanical Engineering Congress and Exposition*, pages 67–74. American Society of Mechanical Engineers, 2012.

[6] M. Labudovic, D. Hu, and R. Kovacevic. A three dimensional model for direct laser metal powder deposition and rapid prototyping. *Journal of Materials Science*, 38(1):35–49, 2003.

[7] Pruk Aggarangsi and Jack L. Beuth. Localized preheating approaches for reducing residual stress in additive manufacturing. In *Proc. SFF Symp., Austin*, pages 709–720, 2006.

[8] Erik R. Denlinger, Jeff Irwin, and Pan Michaleris. Thermomechanical modeling of additive manufacturing large parts. *Journal of Manufacturing Science and Engineering*, 136(6):061007, 2014.

[9] Y. Zhang and K. Chou. A parametric study of part distortions in fused deposition modelling using three-dimensional finite element analysis. *Proceedings of the Institution of Mechanical Engineers, Part B: Journal of Engineering Manufacture*, 222(8):959–968, 2008.

[10] Ahmed Hussein, Liang Hao, Chunze Yan, and Richard Everson. Finite element simulation of the temperature and stress fields in single layers built without-support in selective laser melting. *Materials & Design*, 52:638–647, 2013.

[11] Mahdi Jamshidinia, Fanrong Kong, and Radovan Kovacevic. Numerical modeling of heat distribution in the electron beam melting® of ti-6al-4v. *Journal of Manufacturing Science and Engineering*, 135(6):061010, 2013.

[12] P. Peyre, P. Aubry, R. Fabbro, R. Neveu, and Arnaud Longuet. Analytical and numerical modelling of the direct metal deposition laser process. *Journal of Physics D: Applied Physics*, 41(2):025403, 2008.

[13] Huan Qi, Jyotirmoy Mazumder, and Hyungson Ki. Numerical simulation of heat transfer and fluid flow in coaxial laser cladding process for direct metal deposition. *Journal of Applied Physics*, 100(2):024903, 2006.

[14] R. Rai, JW Elmer, TA Palmer, and T. DebRoy. Heat transfer and fluid flow during keyhole mode laser welding of tantalum, ti–6al–4v, 304l stainless steel and vanadium. *Journal of Physics D: Applied Physics*, 40(18):5753, 2007.

[15] Shaoyi Wen and Yung C. Shin. Modeling of transport phenomena during the coaxial laser direct deposition process. *Journal of Applied Physics*, 108(4):044908, 2010.

[16] Nils Keller and Vasily Ploshikhin. New method for fast predictions of residual stress and distortion of am parts. In *Solid Freeform Fabrication Symposium, Austin, Texas*, pages 1229–1237, 2014.

[17] Pedro Alvarez, Joseba Ecenarro, Iñaki Setien, Maria San Sebastian, Alberto Echeverria, and Luka Eciolaza. Computationally efficient distortion prediction in powder bed fusion additive manufacturing. *Int. J. Eng. Res. Sci*, 2:39–46, 2016.

[18] C Li, CH Fu, YB Guo, and FZ Fang. Fast prediction and validation of part distortion in selective laser melting. *Procedia Manufacturing*, 1:355–365, 2015.

[19] Michael F. Zaeh and Gregor Branner. Investigations on residual stresses and deformations in selective laser melting. *Production Engineering*, 4(1):35–45, 2010.

[20] N. Keller, F. Neugebauer, H. Xu, and V. Ploshikhin. Thermo-mechanical simulation of additive layer manufacturing of titanium aerospace structures. *Proc. DGM Int. Congr. Light Mater*, 2013.

[21] Yukio Ueda, Keiji Fukuda, Keiji Nakacho, and Setsuo Endo. A new measuring method of residual stresses with the aid of finite element method and reliability of estimated values. *Transactions of JWRI*, 4(2):123–131, 1975.

[22] Toshio Mura. *Micromechanics of defects in solids*. Springer Science & Business Media, 2013.

[23] Michael R. Hill and Drew V. Nelson. The inherent strain method for residual stress determination and its application to a long welded joint. *ASME-PUBLICATIONS-PVP*, 318:343–352, 1995.

[24] Peter Mercelis and Jean-Pierre Kruth. Residual stresses in selective laser sintering and selective laser melting. *Rapid Prototyping Journal*, 12(5):254–265, 2006.

[25] Liang Wang and Sergio Felicelli. Process modeling in laser deposition of multilayer ss410 steel. *Journal of Manufacturing Science and Engineering*, 129(6):1028–1034, 2007.

[26] Bo Cheng, Steven Price, James Lydon, Kenneth Cooper, and Kevin Chou. On process temperature in powder-bed electron beam additive manufacturing: Model development and validation. *Journal of Manufacturing Science and Engineering*, 136(6):061018, 2014.

[27] Michael F. Zäh and S. Lutzmann. Modelling and simulation of electron beam melting. *Production Engineering*, 4(1):15–23, 2010.

[28] Nikolay K. Tolochko, Maxim K. Arshinov, Andrey V. Gusarov, Victor I. Titov, Tahar Laoui, and Ludo Froyen. Mechanisms of selective laser sintering and heat transfer in ti powder. *Rapid Prototyping Journal*, 9(5):314–326, 2003.

[29] A.V. Gusarov, Tahar Laoui, Ludo Froyen, and V.I. Titov. Contact thermal conductivity of a powder bed in selective laser sintering. *International Journal of Heat and Mass Transfer*, 46(6):1103–1109, 2003.

[30] Karolien Kempen, Evren Yasa, Lore Thijs, J-P Kruth, and Jan Van Humbeeck. Microstructure and mechanical properties of selective laser melted 18ni-300 steel. *Physics Procedia*, 12:255–263, 2011.

[31] Erik R. Denlinger, Jarred C. Heigel, and Panagiotis Michaleris. Residual stress and distortion modeling of electron beam direct manufacturing ti-6al-4v. *Proceedings of the Institution of Mechanical Engineers, Part B: Journal of Engineering Manufacture*, 229(10):1803–1813, 2015.

[32] Roger Fletcher. *Practical methods of optimization*. John Wiley & Sons, 2013.

[33] Eric Jones, Travis Oliphant, Pearu Peterson, et al. SciPy: Open source scientific tools for Python, 2001–. www.scipy.org, Online; accessed 5 March 2017.

[34] Zhuqing Wang, Erik Denlinger, Panagiotis Michaleris, Alexandru D Stoica, Dong Ma, and Allison M Beese. Residual stress mapping in inconel 625 fabricated through additive manufacturing: Method for neutron diffraction measurements to validate thermomechanical model predictions. *Materials & Design*, 113:169–177, 2017.

[35] Thomas Watkins, Hassina Bilheux, Ke An, Andrew Payzant, Ryan Dehoff, Chad Duty, William Peter, Craig Blue, and Craig A Brice. Neutron characterization for additive manufacturing. 2013.

[36] Yunus A Cengel, Giuliano Dall'Ò, and Luca Sarto. *Termodinamica e trasmissione del calore*. McGraw-Hill, 2013.